Nanoparticle Formation Through Solid-Fed Flame Synthesis: Experiment and Modeling

W. Widiyastuti, Agus Purwanto, Wei-Ning Wang, and Ferry Iskandar
Dept. of Chemical Engineering, Graduate School of Engineering, Hiroshima University, 1-4-1 Kagamiyama, Higashi-Hiroshima 739-8527, Japan

Heru Setyawan
Dept. of Chemical Engineering, Faculty of Industrial Technology, Sepuluh Nopember Institute of Technology, Kampus ITS Keputih Sukolilo, Surabaya 60111, Indonesia

Kikuo Okuyama
Dept. of Chemical Engineering, Graduate School of Engineering, Hiroshima University, 1-4-1 Kagamiyama, Higashi-Hiroshima 739-8527, Japan

DOI 10.1002/aic.11695
Published online March 5, 2009 in Wiley InterScience (www.interscience.wiley.com).

The preparation of silica nanoparticles through solid-fed flame synthesis was investigated experimentally and theoretically. Monodispersed submicrometer- and micrometer-sized silica powders were selected as solid precursors for feeding into a flame reactor. The effects of flame temperature, residence time, and precursor particle size were investigated systematically. Silica nanoparticles were formed by the nucleation, coagulation, and surface growth of the generated silica vapors due to the solid precursor evaporation. Numerical modeling was conducted to describe the mechanism of nanoparticle formation. Evaporation of the initial silica particles was considered in the modeling, accounting for its size evolution. Simultaneous mass transfer modeling due to the silica evaporation was solved in combination with a general dynamics equation solution. The modeling and experimental results were in agreement. Both results showed that the methane flow rate, carrier gas flow rate, and initial particle size influenced the effectiveness of nanoparticle formation in solid-fed flame synthesis. © 2009 American Institute of Chemical Engineers *AIChE J,* 55: 885–895, 2009
Keywords: solid-to-particle conversion, solid particle evaporation, aerosol material processing, silica nanoparticle, population balance method

Introduction

A flame method using gas or liquid feeding materials for particle synthesis is an established industrial process because it can be used for the large-scale production of functional particles ranging in size from nanometers to submicrometers.[1,2] In addition, the particle product usually can be sepa-

Additional Supporting Information may be found in the online version of this article.

Correspondence concerning this article should be addressed to K. Okuyama at okuyama@hiroshima-u.ac.jp.

rated directly from the gas stream without any postprocessing. The commercial process leads to a flame reactor scale-up, which requires a fundamental understanding of operating parameters and particle formation mechanisms.[2–5] This knowledge has been expanded through simulation and modeling processes.[2,6,7]

Most of the reported flame syntheses used gas or liquid as feeding materials.[8] In the case of gas-fed flame synthesis, the mechanism follows gas-to-solid conversion in which particles form by vapor nucleation and grow by particle coagulation and surface growth. Many investigators have reported the modeling of nanoparticle formation following gas-to-solid conversion. A simple approach for the simulation of aerosol dynamics solves the population-balance equation by neglecting the spread of the size distribution.[9–11] A more complex equation, the general dynamic equation (GDE), is a nonlinear partial integro-differential equation developed to calculate particle growth by considering the polydispersity of particle size distribution.[7,12–14] Many previous studies have focused on solving the GDE, with approaches such as the moment method,[15] the sectional method,[16] the discrete sectional method,[17] and the nodal method.[14,18]

A liquid-to-solid conversion in flame synthesis using combustible or volatile precursors has been studied experimentally and theoretically by many groups, including the Pratsinis group.[11,19] A gas-to-particle route usually was applied to the modeling because combustible or volatile precursors lead to extremely fast combustion reactions and evaporation.[1,20] Vapor formation in a liquid-to-solid conversion mechanism has been treated as a "black box" by assuming vapor formation occurs immediately after spraying.[11] In the case of a liquid-fed flame reactor, the liquid precursor in droplet form was sprayed into the reactor. Droplet evaporation and particle dynamics modeling were used to model the flame synthesis process using a volatile precursor.[21] However, the product vapors were treated as the smallest stable particles that formed instantaneously.

Recently, a liquid-fed flame process using nonvolatile precursors, such as aqueous salt solutions, was also reported. Our group reported that YAG:Ce^{3+} submicron-sized particles could be prepared by a liquid-fed flame reactor using sprayed droplets as the precursor.[22] The drying of the droplets due to solvent evaporation and intraparticle reaction occurred during this process. The process was assumed to be analogous to conventional spray pyrolysis (CSP), except that the thermal energy was supplied by a flame rather than an electrical tubular furnace.[20] However, $BaTiO_3$ nanoparticles can be produced in a flame reactor using a droplet precursor, which could not be explained by the mechanism that occurs during the CSP process.[23] Chemical and physical processes accompanying liquid-fed flame synthesis lead to complex analysis of nanoparticle formation.

Even though vapor or volatile liquid-fed flame syntheses have been used in industry, their use is limited to a few materials due to relatively expensive precursors, usually metallic organic chemicals. Nonvolatile liquid-fed flame synthesis is also versatile due to low-cost inorganic salt precursors.[8] Inorganic salt is diluted in a solvent, usually water, before it is sprayed into a flame reactor. However, the energy supplied by the flame is also used to evaporate the solvent, which has a solvent fraction that is higher than that of inorganic salt in the precursor. The present study proposes a one-step process that uses an inexpensive and easy-to-handle bulk material to generate nanoparticles, that is, solid-fed flame synthesis. A solid precursor might be evaporated by a high flame temperature. The generated vapors could result in particle growth by nucleation and coagulation due to a nonisothermal temperature in the flame reactor. To the best our group's knowledge, no published paper has reported a flame synthesis using solid particles as the feeding material sprayed directly into the flame. In addition, the mechanistic analysis is simplified because only physical processes are involved.

In this article, experimental and theoretical silica nanoparticle preparation using solid-fed flame synthesis is reported. Submicrometer- and micrometer-sized silica powders were used as precursors. Theoretical modeling was used to explain the mechanism of nanoparticle formation. Silica solid evaporation is considered before silica vapor nucleation, coagulation, and surface growth, producing silica nanoparticles. The temperature profile and flow field in the flame reactor were included in the dynamics calculation. Parameters, such as methane flow rate, carrier gas flow rate and initial solid silica particles that influence the effectiveness of nanoparticle formation are explained.

Experimental

The experimental system consists of an aerosol generator, a flame burner, and an electrostatic precipitator for collecting particles as shown in Figure 1. It is similar to the experimental system described in our group's previous paper, except for the aerosol generator.[22] An RGB 1000 Solid Particle Disperser (Palas GmbH., Germany) was used as the aerosol generator for supplying solid particles. The piston speed was maintained at 100 mm/h to drive a constant solid particle precursor rate. Monodispersed silica particles of 812 nm and

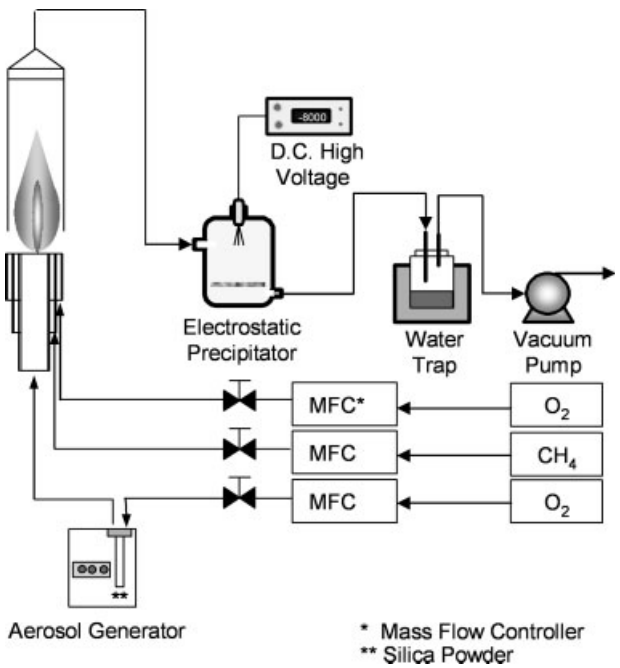

Figure 1. Experimental apparatus.

1912 nm were used (Tokuyama, Tsukuba, Japan). Based on mass balance calculation, 1.67×10^{-4} m^3 s^{-1} of oxygen as a carrier gas can carry 1.4×10^{11} and 1.1×10^{10} particles per m^3 for particles with 812 nm and 1912 nm in diameter, respectively, in the inner flame burner, which is 16 mm in diameter. Methane as a fuel, with a flow rate ranging from 1.67×10^{-5} m^3 s^{-1} to 6.67×10^{-5} m^3 s^{-1} went to the first annular gap of the burner with a thickness of 1.5 mm. The flow rate ratio of oxygen, an oxidizer, to methane was 2.5 to ensure complete combustion. Oxygen, an oxidizer, passed through the second annular gap of the burner. Methane and oxygen flow rates contributed to controlling the temperature distribution in the flame reactor. The flame reactor was covered by a Pyrex glass cylinder that was 96 mm in diameter and 1 m in height.

The generated particles were examined using a field-emission scanning electron microscope (FE-SEM, S-5000, Hitachi Corp., Tokyo, Japan) operated at 20 kV. Random sampling of at least 1000 particles from FE-SEM photographs were examined to reduce limit errors to 2–3% while determining the size distribution of the generated particles.[24]

Numerical Method

First, an appropriate diffusion flame combustion model was selected to obtain the temperature distribution and residence time using computational fluid dynamics (CFD). This result was used to calculate solid evaporation followed by a gas-to-particle conversion calculation using a GDE solution. Modeling is described in detail in the following subsections.

Flame combustion model

Together with continuity, momentum, and energy transport equations, a species transport equation describing the reaction rate in flame combustion was solved. These equations were solved using a commercial CFD code, FLUENT 6.3 (Fluent Asia Pacific, Tokyo, Japan) based on a finite volume technique on a two-dimensional axis-symmetry computational domain. Flame combustion was modeled using a one-step reaction mechanism, assuming complete conversion of the methane as a fuel to CO_2 and H_2O. The turbulence-chemistry interaction was modeled using a generalized eddy-dissipation model.[25] The chemical reaction rate is governed by the large-eddy mixing scale, k/ε. The net rate of the production of species i due to reaction r, $R_{i,r}$, is given by the limiting value of the two expressions below:

$$R_{i,r} = \nu'_{i,r} M_{w,i} A \rho \frac{\varepsilon}{k} \min_{\mathrm{R}} \left(\frac{Y_{\mathrm{R}}}{\nu'_{\mathrm{R},r} M_{w,\mathrm{R}}} \right) \quad (1)$$

$$R_{i,r} = \nu'_{i,r} M_{\mathrm{w},i} A B \rho \frac{\varepsilon}{k} \frac{\sum_P Y_{\mathrm{P}}}{\sum_j^N \nu''_{j,r} M_{\mathrm{w},j}} \quad (2)$$

Y_{P} and Y_{R} are the mass fractions of any product species, P and the mass fraction of a particular reactant, R, respectively. A and B are empirical constants equaling 4.0 and 0.5, respectively. The stoichiometric coefficient for reactant i in reaction r is $\nu'_{i,r}$, and $M_{\mathrm{w},i}$ is the molecular weight of species i.

The standard k-ε model was selected to model turbulence that consists of two transport equations for the turbulence kinetic energy, k, and its dissipation rate, ε, which is stated as follows.[25]

$$\frac{\partial}{\partial t}(\rho k) + \frac{\partial}{\partial x_i}(\rho k u_i) = \frac{\partial}{\partial x_j}\left[\left(\mu + \frac{\mu_{\mathrm{t}}}{\sigma_k} \right) \frac{\partial k}{\partial x_j} \right] + G_{\mathrm{k}} - \rho\varepsilon \quad (3)$$

$$\frac{\partial}{\partial t}(\rho\varepsilon) + \frac{\partial}{\partial x_i}(\rho\varepsilon u_i) = \frac{\partial}{\partial x_j}\left[\left(\mu + \frac{\mu_{\mathrm{t}}}{\sigma_\varepsilon} \right) \frac{\partial \varepsilon}{\partial x_j} \right] + C_{1\varepsilon} \frac{\varepsilon}{k} G_{\mathrm{k}} - C_{2\varepsilon} \rho \frac{\varepsilon^2}{k} \quad (4)$$

G_{k} is the generation of turbulence kinetic energy due to mean velocity gradients. The turbulent viscosity (μ_{t}) is defined by $\mu_{\mathrm{t}} = \rho C_\mu k^2/\varepsilon$. The values of the model parameters are $C_{1\varepsilon} = 1.44$, $C_{2\varepsilon} = 1.92$, $C_\mu = 0.09$, $\sigma_{\mathrm{k}} = 1.0$, and $\sigma_\varepsilon = 1.3$. This calculation generated temperature profiles and flow fields in the flame reactor that were used to calculate particle evaporation, and regeneration or growth. Particle evolution was assumed following a symmetric four-path line flow beginning from the precursor inlet in the burner surface. The silica particle fraction in each path line was calculated based on the assumption that a homogenous solid precursor was distributed in the precursor inlet.

The temperature profile obtained from the CFD simulation was validated using thermocouple measurements taken along the axis line, as shown in Figure S1 of the supporting information. The methane flow rate as fuel was 3.33×10^{-5} m^3 s^{-1}. The flow rate ratio of oxygen (oxidizer) to methane was 2.5. Nitrogen at a flow rate of 3.33×10^{-5} m^3 s^{-1} was used as the carrier gas.

Evaporation of silica solid particles

Silica particle evaporation modeling was treated in a similar manner to metal oxide evaporation in which vapor pressure was substantial enough to cause metal oxide to evaporate.[26] The modeling also was similar to the droplet evaporation which was used in our group's previous studies to explain the decrease in droplet size due to solvent evaporation in spray pyrolysis processes.[27,28] The change in particle diameter, d_{p}, and silica vapor number concentration, $N(1)$, were calculated based on material balance equations. These equations are used when the saturation ratio is less than 1. The change of the silica particle diameter, due to particle evaporation, is:

$$\frac{dd_{\mathrm{p}}}{dt} = \frac{4 D_{\mathrm{v}} m_1}{\rho_{\mathrm{p}} d_{\mathrm{p}}} (N(1) - n_s) \quad (5)$$

The change of silica vapor concentration in the surrounding gas is:

$$\frac{dN(1)}{dt} = -2\pi d_{\mathrm{p}} D_{\mathrm{v}} N_{\mathrm{o}} (N(1) - n_{\mathrm{s}}) \quad (6)$$

Particle reforming is due to the nucleation process of silica vapor when its concentration is greater than its saturation concentration, n_{s}, which is shown by:

$$n_s = \frac{P_{\mathrm{s}}}{k_{\mathrm{B}} T} \quad (7)$$

where p_{s} is saturated vapor pressure. The required data properties were taken from Perry's chemical engineering handbook.[29]

Silica nanoparticle formation

Modeling of gas-to-particle conversion involves nucleation, condensation of vapors onto the particles and coagulation between the particles. Vapors nucleate when the saturation condition is surpassed either by decreasing the temperature or increasing the vapor concentration.[9] If the saturation ratio, $N(1)/n_s$ is greater than or equals to 1, the calculation based on the gas-to-particle conversion mechanism is initiated. Supersaturation occurs when the saturation ratio is sufficient for vapors to nucleate. According to the classical nucleation theory, nucleation occurs, forming stable clusters at a sufficient supersaturation value that results when the critical particle volume, v^*, is greater than the monomer volume, v_1.[20] The supersaturation value also influences the rate of nucleation, J(k).

In the modeling, the particles are assumed to be spherical and electrically neutral. Particles collision is assumed, forming a single new spherical particle. The simplified model of the sectional approach to discretize the particle size distribution, called the nodal method, was used to model the gas-to-particle conversion in flame synthesis.[14,18] It evolves nucleation, coagulation, and surface growth of supersaturated vapor, which is written in the population balance equation as follows:

$$\frac{dN(k)}{dt} = \left.\frac{dN(k)}{dt}\right|_{\text{nucl}} + \left.\frac{dN(k)}{dt}\right|_{\text{coag}} + \left.\frac{dN(k)}{dt}\right|_{\text{evap/cond}} \tag{8}$$

$$\left.\frac{dN(k)}{dt}\right|_{\text{nucl}} = J(k)\xi(k) \tag{9}$$

$$\left.\frac{dN(1)}{dt}\right|_{\text{nucl}} = -J(k)k^* \tag{10}$$

$$\xi(k) = \begin{cases} \frac{v^*}{v(k)}; \text{ if } v(k-1) \le v^* \le v(k) \\ \frac{v^*}{v(2)}; \text{ if } v^* \le v_1 \\ 0; \text{ otherwise} \end{cases} \tag{11}$$

$$v^* = \frac{\pi}{6}\left(\frac{4\sigma v_1}{k_B T \ln S}\right)^3 \tag{12}$$

$\xi(k)$ is the size operator that puts the nucleated particle at the node just larger than its critical size node, k^*, which is defined as:

$$k^* = \left(\frac{2s_1\sigma}{3k_B T \ln S}\right)^3 \tag{13}$$

The classical homogenous nucleation theory with self-consistent correction (SCC) was applied as follows:

$$J(k) = n_s^2 S v_1 \left(\frac{2\sigma}{\pi m_1}\right)^{0.5} \exp\left(\frac{s_1\sigma}{k_B T} - \frac{4\left(s_1\sigma/k_B T\right)^3}{27\log^2 S}\right) \tag{14}$$

Coagulation refers to the collision of two particles larger than the critical size node k^*. The correlation for collision frequency function, $\beta(i,j)$, was determined by:

$$\beta(i,j) = \left(\frac{3}{4\pi}\right)^{1/6}\left(\frac{6k_B T}{\rho_p}\right)^{1/2}\left(\frac{1}{v(i)}+\frac{1}{v(j)}\right)^{1/2}\left(v(i)^{1/3}+v(j)^{1/3}\right)^2 \tag{15}$$

The rate of change of the particle size distribution due to coagulation is shown by:

$$\left.\frac{dN(k)}{dt}\right|_{\text{coag}} = \frac{1}{2}\sum_{\substack{i=2\\ j=2}} \chi(i,j,k)\beta(i,j)N(i)N(j) - N(k)\sum_{i=2}\beta(i,j)N(i) \tag{16}$$

where $\chi(i,j,k)$ is a size operator due to coagulation, which is defined as follows:

$$\chi_{ijk} = \begin{cases} \frac{v(k+1)-(v(i)+v(j))}{v_{k+1}-v_k}; \text{ if } v(k) \le v(i)+v(j) \le v(k+1) \\ \frac{(v(i)+v(j))-v(k-1)}{v(k+1)-v(k)}; \text{ if } v(k-1) \le v(i)+v(j) \le v(k) \\ 0; \text{ otherwise} \end{cases} \tag{17}$$

Particles can grow due to the condensation of monomers to the particle surface called surface growth. They also can evaporate from the surface depending on the vapor pressure difference and the Kelvin effect. The change in particle size distribution due to surface growth can be stated as:

$$\left.\frac{dN(k)}{dt}\right|_{\text{evap/cond}} = \begin{cases} \frac{v(1)}{v(k)-v(k-1)}\beta(1,k-1)(N(1)-N(1,k-1)^s)N(k-1) \\ \qquad \text{if } N(1) > N(1,k-1)^s \\ -\frac{v(1)}{v(k+1)-v(k)}\beta(1,k+1)(N(1)-N(1,k+1)^s)N(k+1) \\ \qquad \text{if } N(1) < N(1,k+1)^s \\ -\frac{v(1)}{v(k+1)-v(k)}\beta(1,k)(N(1)-N(1,k)^s)N(k) \\ \qquad \text{if } N(1) > N(1,k)^s \\ \frac{v(1)}{v(k)-v(k-1)}\beta(1,k)(N(1)-N(1,k)^s)N(k) \\ \qquad \text{if } N(1) < N(1,k)^s \end{cases} \tag{18}$$

$$\left.\frac{dN(1)}{dt}\right|_{\text{evap/cond}} = \begin{cases} -\beta(1,k-1)(N(1)-N(1,k-1)^s)N(k-1) \\ \qquad \text{if } N(1) > N(1,k-1)^s \\ -\beta(1,k+1)(N(1)-N(1,k+1)^s)N(k+1) \\ \qquad \text{if } N(1) < N(1,k+1)^s \\ -\beta(1,k)(N(1)-N(1,k)^s)N(k) \\ \qquad \text{if } N(1) > N(1,k)^s \\ -\beta(1,k)(N(1)-N(1,k)^s)N(k) \\ \qquad \text{if } N(1) < N(1,k)^s \end{cases} \tag{19}$$

All variables, such as $N(1)$ and N(k), were calculated as functions of temperature and time along the flame reactor obtained from the temperature and velocity profiles measured using CFD. Temperature profile as a function of position, x,

was obtained from the CFD simulation. The correlation between time, t, and distance, x, is described by $dx = v(x)dt$ or $dt = \frac{1}{v(x)}dx$, where $v(x)$ also is obtained from the CFD simulation.

Results and Discussion

Temperature distribution and particle path lines

Based on the CFD calculations, two-dimensional temperature profiles and flow fields can be obtained. Figure 2a–d shows the temperature profiles for methane flow rates ranging from 1.67×10^{-5} to 6.67×10^{-5} m^3 s^{-1} along the flame reactor. The temperature increased with an increased in methane flow rate, producing a larger flame region. This result was consistent with experimental results of our previous study.[30] The flow field was stated as path lines of carrier gas flow entering the flame reactor through the precursor inlet. The carrier gas flow dispersed to the flame reactor undergoes a translation flow in both the axial and the radial direction, as shown by each path line in Figure 2e. Each path has a slightly different temperature distribution, depending on its distance from the reactor axis, as shown in Figure 3. Silica particles were assumed following these paths with number fractions in proportion to the surface area of each path in the precursor inlet. The path that is farthest from the reactor axis (e.g., path line 4) has a higher temperature and faster cooling rate than those of the path nearest the reactor axis (e.g., path line 1). This result is similar to Johannesen's simulation result, which also used a particle trajectory approach.[31] The temperature distribution in the flame reactor can be divided into two zones that characterize heating and cooling. Heating and cooling zones contributed to the evaporation stage and the transformation of vapor to particles, respectively. It can be shown that the heating zone has a much shorter length than the cooling zone. For example, the lengths of the heating zones following path line 1 for a methane flow rate of 1.67×10^{-5}, 3.33×10^{-5}, 5.00×10^{-5} and 6.67×10^{-5} m^3 s^{-1} are about 0.05, 0.1, 0.15, and 0.2 m, respectively, from the burner surface. The increase in methane flow rate was followed by an increase in maximal temperature at approximately 1000, 1500, 1900, and 2200 K. It is possible the initial silica particles cannot fully evaporate, resulting in final particles with an unchanged size. This will be discussed in the following subsection.

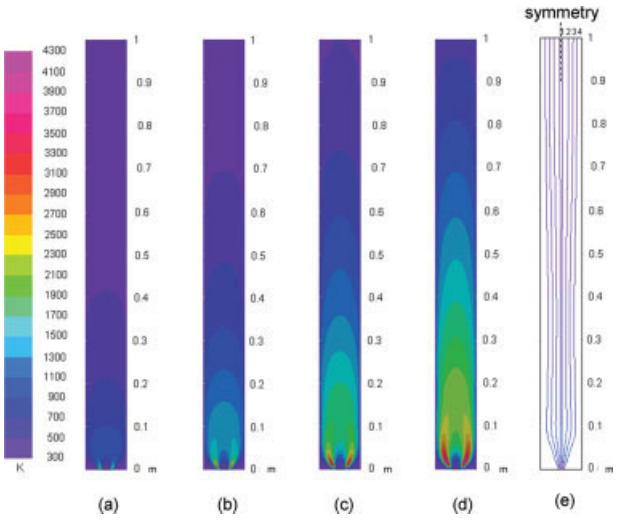

Figure 2. Temperature distribution along the flame reactor calculated by CFD for a methane flow rate of (a) 1.67×10^{-5}, (b) 3.33×10^{-5}, (c) 5.00×10^{-5}, and (d) 6.67×10^{-5} m^3 s^{-1}, (e) temperature path line of condition (a).

[Color figure can be viewed in the online issue, which is available at www.interscience.wiley.com.]

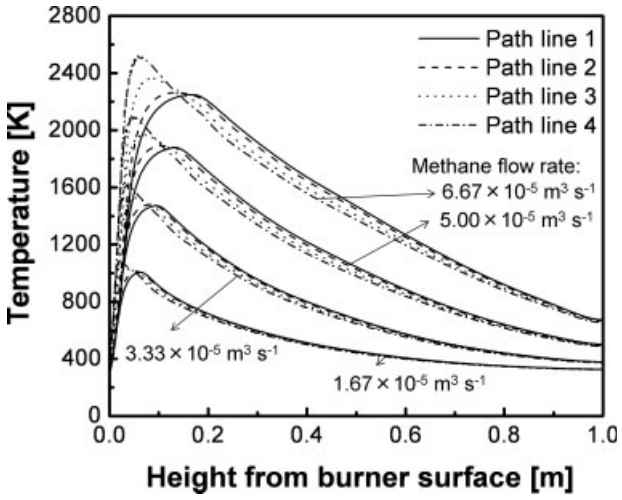

Figure 3. Temperature distribution along the flame reactor at each path line with a methane flow rate of 1.67×10^{-5}, 3.33×10^{-5}, 5.00×10^{-5}, and 6.67×10^{-5} m^3 s^{-1}.

The effect of methane flow rate

Figure 4a shows FE-SEM images of monodispersed precursor particles 812 nm in diameter. The evolution of particle size from submicron-sized particles to nanoparticles depends on the methane flow rate, which is influenced by the temperature distribution in the flame reactor. Using a methane flow rate of 1.67×10^{-5} m^3 s^{-1}, the initial particle size slightly decreased, and the condensation of silica vapor on the silica surface was observed as shown in Figure 4b. The simulation result, as shown in Figure 5a, was in accordance with the measurement. The initial particles barely evaporated, and the product particle size was very similar to the initial particle size. In the case of the methane flow rate of 3.33×10^{-5} m^3 s^{-1}, most submicrometer silica particles fully evaporated to generate nanoparticles as shown in Figure 4c. Some particles could not fully evaporate because of the inhomogeneous temperature distribution in both the axial and radial positions, as explained above. The simulation result agreed with the particle size distribution measurement, as shown in Figure 5b. The bimodal size distribution can be explained by the simulation result. From the simulation, the evolution particle size that followed the outer path line of the temperature distribution (path line 4) evaporated completely. However, at other path lines, the initial silica particles evaporated incompletely. This is because the temperature in the outer path line is higher than the center. In the case of the methane flow

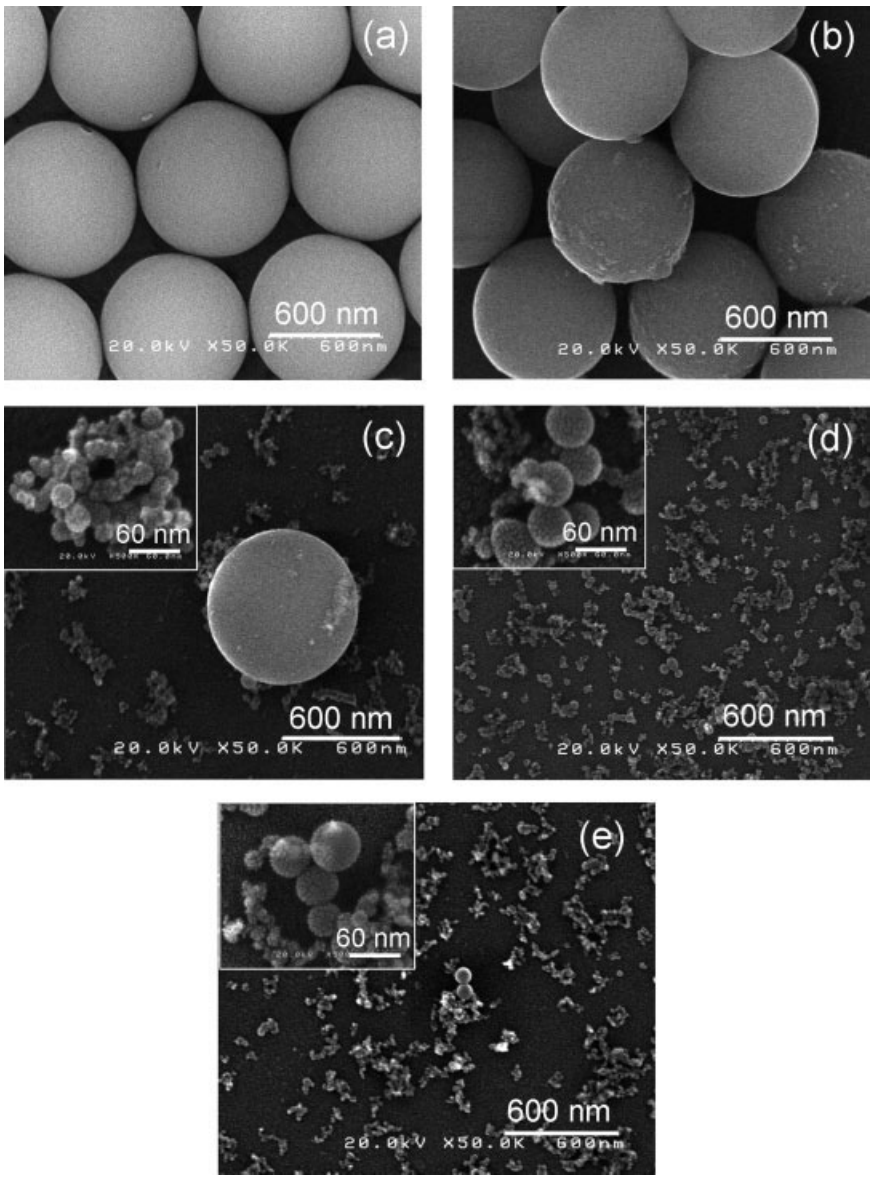

Figure 4. FE-SEM images of (a) initial silica particles size of 812 nm selected as precursor, particles in the collector after treatment in the flame reactor carried by 1.67 × 10^{-4} m^3 s^{-1} oxygen with a methane flow rate of (b) 1.67 × 10^{-5}, (c) 3.33 × 10^{-5}, (d) 5.00 × 10^{-5}, and (e) 6.67 × 10^{-5} m^3 s^{-1}.

Insets show high magnification of FE-SEM images.

rates of 5.00 × 10^{-5} and 6.67 × 10^{-5} m^3 s^{-1}, all initial silica particles transformed to silica nanoparticles as shown in Figure 4d,e. Nanoparticles formed by evaporation of silica at higher flame temperatures. The process continued to nucleation and particle growth when supersaturation occurred. The agreement between the generated particle size distribution obtained by simulation and measurement is shown in Figure 5c,d.

The size evolution of silica particles from burner surface to reactor outlet along the reactor axis for methane flow rates of 5.00 × 10^{-5} and 6.67 × 10^{-5} m^3 s^{-1} is shown in Figure 6a,b. For a methane flow rate of 5.00 × 10^{-5} m^3 s^{-1}, particle size decreased from an initial value of 812 nm to 560 nm at 0.1 m from the burner surface in 0.08 s. All particles fully evaporated to generate silica vapors or silica monomers at 0.15 m from the burner surface in 0.12 s. Figure 6a shows that the gas phase was maintained up to ~0.4 m, at which distance silica particle began to appear. This occurred in 0.38 s and the smallest particle was 1.06 nm, which was larger than the monomer size (0.53 nm). Silica particles reformed by nucleation, coagulation, and surface growth when the silica vapor reached supersaturation.

The particle mass concentration along the axis of the reactor (0.0625 total number of initial silica particles) at a methane flow rate of 5.00 × 10^{-5} m^3 s^{-1} and an oxygen carrier gas flow rate of 1.67 × 10^{-4} m^3 s^{-1} and an initial particle size of 812 nm is shown in the supporting information (Figure S3 and Table S1). The particle mass concentration was calculated from the area under the curve, $m = \sum_{i=2}^{n} \rho v(k) N(k)$. Table S1 shows that the particle mass

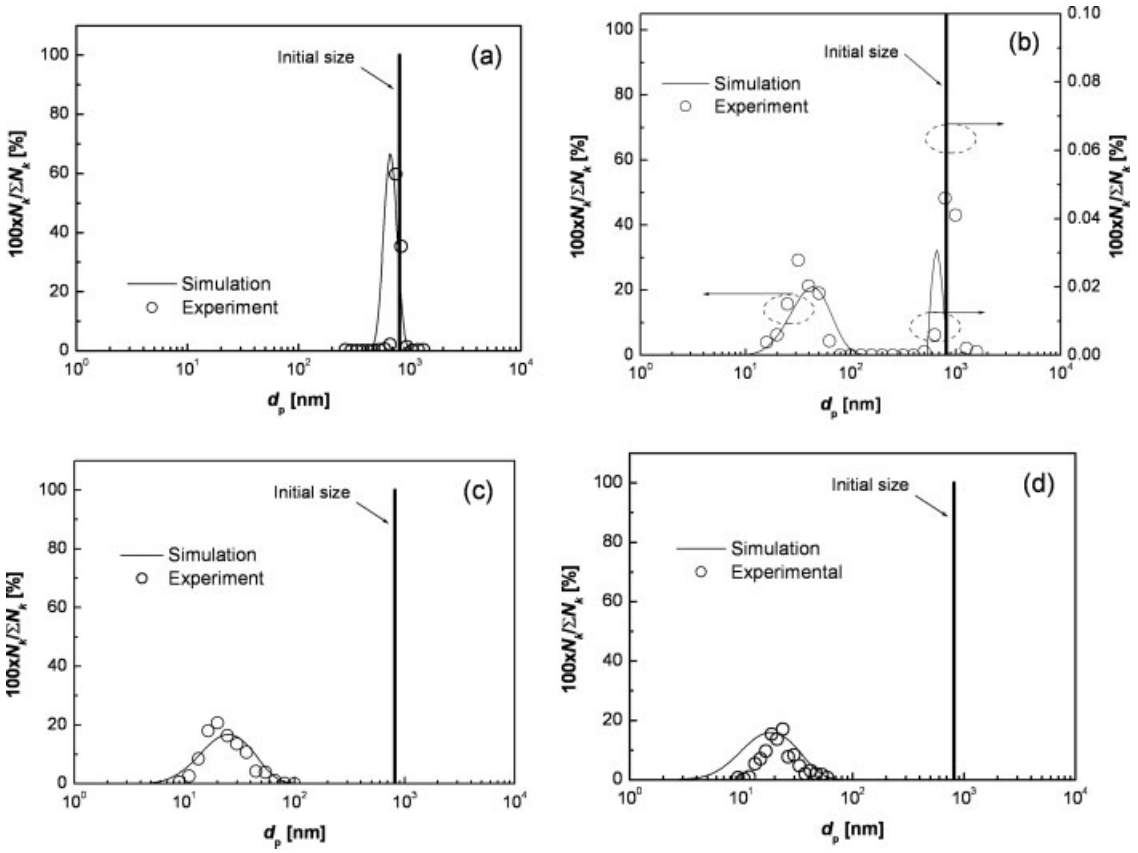

Figure 5. Particle size distribution from simulation and experiment taken from FE-SEM images.

Operation condition: 1.67×10^{-4} m^3 s^{-1} oxygen with a methane flow rate of (a) 1.67×10^{-5}, (b) 3.33×10^{-5}, (c) 5.00×10^{-5}, and (d) 6.67×10^{-5} m^3 s^{-1}.

concentration was regained at a distance from the burner surface of approximately 0.7 m. Particle mass concentration decreased from 6.3×10^{-6} to 4.4×10^{-13} kg m^{-3} in the range of 0 to 0.4 m from the burner surface due to evaporation. The increase in particle mass concentration from 4.4×10^{-13} to 6.3×10^{-6} kg m^{-3} in the range of 0.4 to 0.7 m is shown the Figure S3 and the Table S1.

By using a methane flow rate of 6.67×10^{-5} m^3 s^{-1}, faster evaporation was demonstrated in the simulation results, as shown in Figure 6b. At 0.1 m from the burner surface (0.06 s), full evaporation occurred. The regeneration of silica particles was initiated at about 0.6 m from the burner surface (0.49 s); the smallest particle size was 1.33 nm. The silica vapor condition occupied a longer distance in the reactor at a higher methane flow rate rather than a lower flow rate. The times needed for final particles to reach 1 m from the burner surface using methane flow rates of 5.00×10^{-5} and 6.67×10^{-5} m^3 s^{-1} were 1.73 and 117 s, respectively.

The effect of precursor particle size

Figure 7a shows FE-SEM images of the silica particles generated by a flame reactor with an initial particle size of 1912 nm. An oxygen (carrier gas) flow rate of 1.67×10^{-4} m^3 s^{-1} and a methane (fuel) flow rate of 5.00×10^{-5} m^3 s^{-1} were used. The vapor number concentration, $N(1)$ is defined by the population balance equation that can be obtained by simultaneously solving Eqs. 5–19, that account for both evaporation of initial silica particles and regeneration silica nanoparticles, that is, the nucleation, coagulation, and surface growth (re-evaporation/condensation) processes. Nanoparticles were generated along with particles from the incomplete evaporation of initial silica particles. Nanoparticles generated from particles with an initial size of 1912 nm were smaller than those generated from the 812-nm particles. This is because the rate of evaporation decreased and the silica vapor number concentration increased in accordance with the increase in particle size as indicated by Eqs. 5–6. In a conventional spray pyrolysis system, the solvent evaporation time also increases with the droplet size.[27] Therefore, an increase in initial particle size requires more time for silica to attain complete evaporation. The vapor number concentration generated by larger particles was reduced because incomplete evaporation occurred. This resulted in a reduction in nanoparticle formation due to coagulation and surface growth.

The simulation results predicted that near the flame reactor axis, evaporation of the precursor is incomplete. However, far from the flame reactor axis, full evaporation occurs. This resulted in a bimodal size distribution of the final particles, as shown in Figure 7b. In this case, supersaturation was reached before full evaporation of silica occurred. Surface

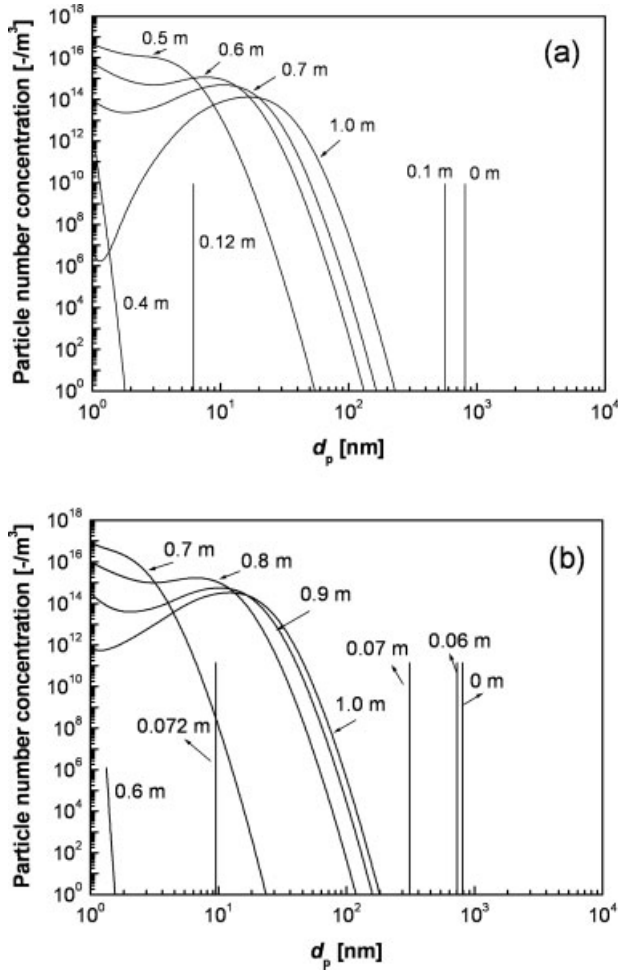

Figure 6. Particle size evolution from burner surface to reactor outlet at the reactor axis.

Operation condition: 1.67×10^{-4} m^3 s^{-1} oxygen with a methane flow rate of (a) 5.00×10^{-5} and (b) 6.67×10^{-5} m^3 s^{-1}.

growth by condensation/evaporation occurs both on particles that experienced incomplete evaporation and on nanoparticles that formed by nucleation and coagulation, which was treated based on the size range or nodal in the calculation. The geometric mean diameter and the standard deviation of nanoparticles by prediction were 19.5 nm and 1.8. The measurements resulted in a 16.6 nm geometric mean diameter and a 1.6 standard deviation.

The effect of carrier gas flow rate

To investigate the effect of carrier gas, the methane flow rate and the initial precursor size are kept constant at 5.00×10^{-5} m^3 s^{-1} and 812 nm, respectively. Figure 8a shows the FE-SEM images of particles using a carrier gas flow rate of 6.67×10^{-5} m^3 s^{-1}. Nonagglomerated nanoparticles can be generated, which indicates that the precursor fully evaporated and subsequent particle growth by a gas-to-particle mechanism occurred. The decrease in the carrier gas flow rate led to the increase of temperature and residence time in the flame reactor. On the other hand, increasing the carrier gas flow rate to 2.17×10^{-4} m^3 s^{-1} generated agglomerated nanoparticles with a smaller size, as shown in Figure 8b. Submicrometer particles from barely evaporated precursor were still observed, indicating that the temperature and residence time were not enough to evaporate the precursor completely.

CFD analysis, as shown in Figure 9, also indicates that the maximum reactor temperature along the axis flame reactor decreased from 2700 K to 1600 K by increasing the carrier gas flow rate from 6.67×10^{-5} to 2.17×10^{-4} m^3 s^{-1}. The residence time also decreased from 3.3 s to 1.5 s. The temperature relative to the silica particle melting point led to the nucleated particles colliding and fusing, quickly generating spherical nanoparticles.[32] In addition, the residence time was long enough for particle collision that is effective in high temperatures. In contrast, the higher flow rate of carrier gas tended to cool the flame temperature and dilute the concentration of the precursor, generating smaller particle size.[11]

The simulation result is in accordance with the experimental work for the carrier gas flow rate of 6.67×10^{-5} m^3 s^{-1} as shown in Figure 10a. The geometric mean diameter of the simulation and experiment results are 40.3 nm and 38.0 nm,

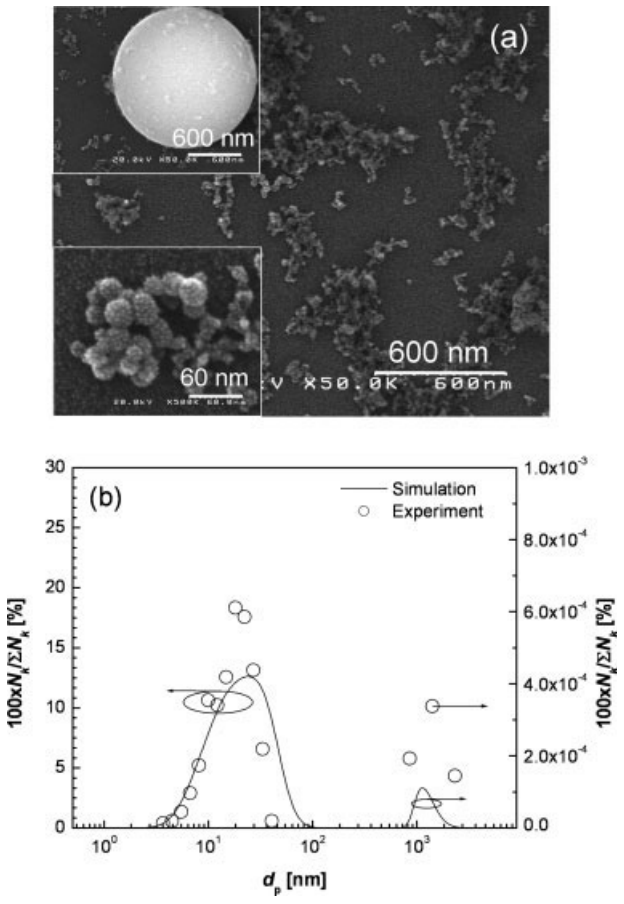

Figure 7. (a) FE-SEM images of particles, (b) size distribution of particles generated by flame reactor carried by 1.67×10^{-4} m^3 s^{-1} with oxygen as the carrier gas and a methane flow rate of 5.00×10^{-5} m^3 s^{-1} using an initial silica size of 1912 nm.

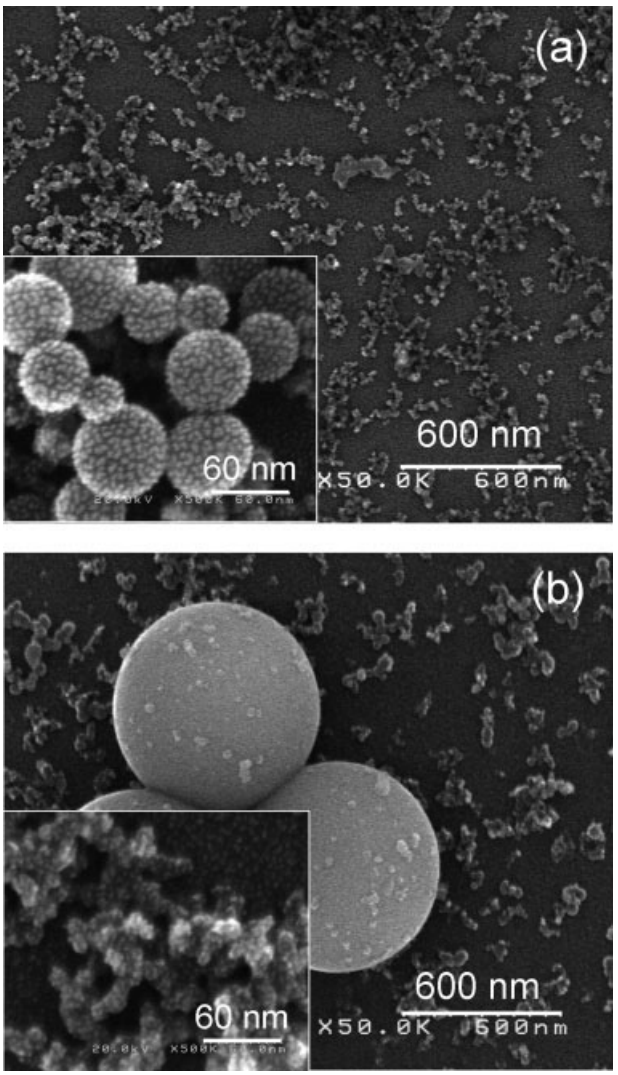

Figure 8. FE-SEM images of particles generated by flame reactor carried by (a) 6.67 × 10^{-5} and (b) 2.17 × 10^{-4} m^3 s^{-1} with oxygen as the carrier gas and a methane flow rate of 5.00 × 10^{-5} m^3 s^{-1} as fuel and an initial precursor size of 812 nm.

Insets show high magnification of FE-SEM images.

with a standard deviation of 1.7 and 1.5, respectively. The experiment and simulation results for particles generated using a carrier gas flow rate of 2.17 × 10^{-4} m^3 s^{-1} are shown in Figure 10b. The geometric mean diameter of the simulation results for nanoparticle generation is 8.6 nm with a standard deviation of 2.1, whereas the geometric mean diameter of the experiment result is 9.5 nm with a standard deviation of 1.4.

Suggested mechanism of particle size evolution in flame reactor using solid precursor

Based on the discussion above, a mechanism for particle size evolution in flame synthesis using a solid precursor is proposed. The schematic illustration for the mechanism of

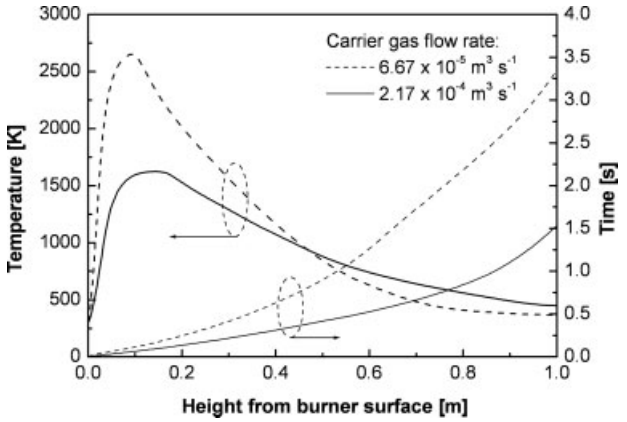

Figure 9. Temperature profile and residence time along the reactor axis using oxygen as the carrier gas with a flow rate of 6.67 × 10^{-5} and 2.17 × 10^{-4} m^3 s^{-1} using a methane flow rate of 5.00 × 10^{-5} m^3 s^{-1}.

particle formation in flame synthesis using solid particles as a precursor is shown in Figure 11. There are three possibilities for particles generated using submicron-micron-sized solid particles as precursors: nanoparticles, nanoparticles

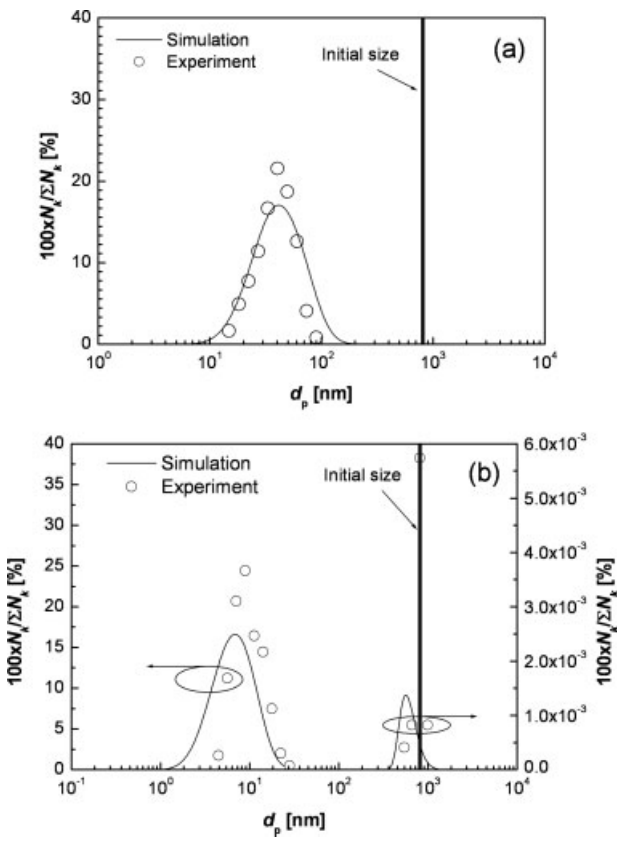

Figure 10. Particle size distribution generated by flame reactor using oxygen as the carrier gas with a flow rate of (a) 6.67 × 10^{-5} and (b) 2.17 × 10^{-4} m^3 s^{-1} and a methane flow rate of 6.67 × 10^{-5} m^3 s^{-1} and a precursor size of 812 nm.

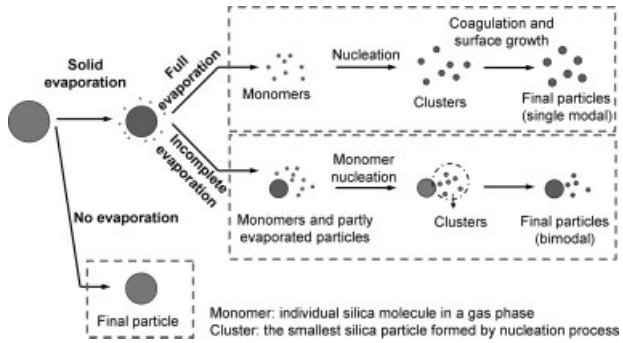

Figure 11. Particle formation illustration of solid-fed flame synthesis.

combined with particles relatively unchanged in size and particles relatively unchanged in size. The generated particles depend on the parameters discussed above. Nanoparticle generation is started by evaporating a solid precursor to produce vapors or monomers (molecules). Particle reformation is caused by nucleation of vapors when supersaturation occurs either by increasing vapor concentration or decreasing the temperature. The first particles generated by the nucleation process are called clusters. The clusters can grow further by coagulation with other clusters or particles and condensation with monomers. This mechanism is known as gas-to-particle conversion.[20] Occasionally, supersaturation occurs when the evaporation of solid precursor is not complete, producing a bimodal size distribution. This occurs when the submicrometer-micrometer sized particles are smaller than the original particles and nanoparticles arise from gas phase particle synthesis. Particle size remains relatively unchanged when the initial particles barely evaporate. This is due to the surrounding temperature being low enough to evaporate the initial particles. The generated particles can be obtained through modeling by considering both solid evaporation and gas-to-particle conversion.

Conclusions

Silica nanoparticles were generated through submicrometer-micrometer sized solid-fed flame synthesis. The model explaining the proposed mechanism also was presented. The suggested modeling involved two routes: solid evaporation for silica vapor generation and a gas-to-particle conversion to generate silica nanoparticles from vapor nucleation, coagulation and surface growth mechanisms. The results showed that the flame temperature increased with an increasing methane flow rate as fuel that can control the evaporation stage and the gas-to-particle conversion stage. For a methane flow rate of 1.67×10^{-5} m^3 s^{-1}, the initial particle size was minimally reduced. However, using a methane flow rate of 6.67×10^{-5} m^3 s^{-1}, silica nanoparticles can be produced. Increasing the carrier gas flow rate leads to the decreasing temperature flame and residence time, producing smaller nanoparticles together with an incompletely evaporated precursor. Nonagglomerated and larger nanoparticles were obtained using a carrier gas flow rate as low as 6.67×10^{-5} m^3 s^{-1}. By increasing the precursor particle size from 812 nm to 1912 nm, while other conditions remained constant, the evaporation rate decreased, producing smaller nanoparticles together with barely evaporated particles. The modeling results describe the mechanism of nanoparticle synthesis in a flame reactor using a solid precursor, which was supported by experimental work.

Acknowledgments

The authors wish to thank Nguyen Thi My Diep for assistance in experimental work and Tokuyama Co. Ltd., Tsukuba, Japan, for providing silica particles. The Ministry of Education, Culture, Sports, Science, and Technology (MEXT) of Japan (W.W. and A. P.) are acknowledged for providing doctoral scholarships.

Notation

A = an empirical constant equal to 4.0
B = an empirical constant equal to 0.5
$C_{1\varepsilon}$ = the first constant in the dissipation energy equation
$C_{2\varepsilon}$ = the second constant in the dissipation energy equation
C_μ = the constant of the turbulent viscosity
d_p = particle diameter, m
G_k = the generation of turbulence kinetic energy due to mean velocity gradients, J m^{-3} s^{-1}
$J(k)$ = nucleation rate, m^{-3} s^{-1}
k = turbulence kinetic energy, m^2 s^{-2}
k^* = the critical size node
k_B = Boltzmann constant, J K^{-1}
$M_{w,i}$ = molecular weight of species i, kg mol^{-1}
m_1 = mass of a silica molecule, kg
$N(1)$ = silica vapor number concentration, m^{-3}
$N(k)$ = number concentration of silica particles at the kth node, m^{-3}
$N^s_{1,k}$ = number concentration of monomers over a k sized particle at saturation, m^{-3}
N_o = initial silica particle number concentration, m^{-3}
n_s = saturated silica vapor concentration, molecules m^{-3}
p_s = saturated pressure, N m^{-2}
$R_{i,r}$ = the net rate of production of species i due to reaction r, kg m^{-3} s^{-1}
S = saturation ratio
s_1 = surface of a silica molecule, m^2
T = temperature, K
t = time, s
u_i = velocity components, m s^{-1}
$v(k)$ = volume of particles at the kth node, m^3
v^* = critical volume of particle, m^3
v_1 = volume of a silica molecule, m^3
$v'_{i,r}$ = stoichiometric coefficient for reactant i in the reaction r
$v''_{j,r}$ = stoichiometric coefficient for product j in the reaction r
x_i = coordinate direction, m
Y_P = the mass fraction of any product species P
Y_R = the mass fraction of particular reactant R

Greek letters

B = collision frequency function
$\chi(i,j,k)$ = size operator due to coagulation at the kth node
ε = dissipation rate of turbulent kinetic energy, m^2 s^{-3}
μ = gas viscosity, kg m^{-1} s^{-1}
μ_t = the turbulent viscosity, kg m^{-1} s^{-1}
ρ = gas density, kg m^{-3}
ρ_p = particle density, kg m^{-3}
σ = surface tension, N m^{-1}
σ_k = turbulent Prandtl number for k
σ_ε = turbulent Prandtl number for ε
$\xi(k)$ = size operator due to nucleation at the kth node

Literature Cited

1. Pratsinis SE. Flame aerosol synthesis of ceramic powders. *Prog Energy Combust Sci*. 1998;24:197–219.

2. Roth P. Particle synthesis in flame. *Proc Combust Inst*. 2007;31:1773–1788.
3. Dittmann R, Richter J, Vital A, Piazza D, Aneziris C, Graule T. Influence of burner scale-up on characteristics of flame-synthesized titania and silica nanoparticles. *Adv Eng Mater*. 2005;7:354–360.
4. Wegner K, Pratsinis SE. Scale-up of nanoparticle synthesis in diffusion flame reactors. *Chem Eng Sci*. 2003;58:4581–4589.
5. Mueller R, Madler L, Pratsinis SE. Nanoparticle synthesis at high production rates by flame spray pyrolysis. *Chem Eng Sci*. 2003;58:1969–1976.
6. Kammler HK, Madler L, Pratsinis SE. Flame synthesis of nanoparticles. *Chem Eng Technol*. 2001;24:583–596.
7. Schild A, Gutsch A, Muhlenweg H, Pratsinis SE. Simulation of nanoparticle production in premixed aerosol flow reactors by interfacing fluid mechanics and particle dynamics. *J Nanoparticle Res*. 1999;1:305–315.
8. Strobel R, Pratsinis SE. Flame aerosol synthesis of smart nanostructured materials. *J Mater Chem*. 2007;17:4743–4756.
9. Panda S, Pratsinis SE. Modeling the synthesis of aluminum particles by evaporation-condensation in an aerosol flow reactor. *Nanostruct Mater*. 1995;5:755–767.
10. Kruis FE, Kusters KA, Pratsinis SE, Scarlett B. A simple model for the evolution of the characteristics of aggregate particles undergoing coagulation and sintering. *Aerosol Sci Technol*. 1993;19:514–526.
11. Mueller R, Jossen R, Kammler HK, Pratsinis SE. Growth of zirconia particles made by flame spray pyrolysis. *AIChE J*. 2004;50:3085–3094.
12. Muhlenweg H, Gutsch A, Schild A, Pratsinis SE. Process simulation of gas-to-particle-synthesis via population balances: investigation of three models. *Chem Eng Sci*. 2002;57:2305–2322.
13. Gutsch A, Muhlenweg H, Kramer M. Tailor-made nanoparticles via gas-phase synthesis. *Small*. 2005;1:30–46.
14. Prakash A, Bapat AP, Zachariah MR. A simple numerical algorithm and software for solution of nucleation, surface growth, and coagulation problems. *Aerosol Sci Technol*. 2003;37:892–898.
15. Pratsinis SE. Simultaneous nucleation, condensation, and coagulation in aerosol reactors. *J Colloid Interface Sci*. 1988;124:416–427.
16. Gelbard F, Seinfeld H. Simulation of multicomponent aerosol dynamics. *J Colloid Interface Sci*. 1980;78:485–501.
17. Okuyama K, Kousaka Y, Tohge N, Yamamoto S, Wu JJ, Flagan RC, Seinfeld JH. Production of ultrafine metal oxide aerosol particles by thermal decomposition of metal alkoxide vapors. *AIChE J*. 1986;32:2010–2019.
18. Lehtinen KEJ, Zachariah MR. Self-preserving theory for the volume distribution of particles undergoing brownian coagulation. *J Colloid Interface Sci*. 2001;242:314–318.
19. Madler L, Kammler HK, Mueller R, Pratsinis SE. Controlled synthesis of nanostructured particles by flame spray pyrolysis. *J Aerosol Sci*. 2002;33:369–389.
20. Kodas TT, Hampden-Smith MJ. *Aerosol Processing of Materials*. New York: Wiley-VCH, 1999.
21. Heine MC, Pratsinis SE. Droplet and particle dynamics during flame spray synthesis of nanoparticles. *Ind Eng Chem Res*. 2005;44:6222–6232.
22. Purwanto A, Wang WN, Lenggoro IW, Okuyama K. Formation and luminescence enhancement of agglomerate-free YAG:Ce^{3+} submicrometer particles by flame-assisted spray pyrolysis. *J Electrochem Soc*. 2007;154:J91–J96.
23. Purwanto A, Wang WN, Lenggoro IW, Okuyama K. Formation of $BaTiO_3$ nanoparticles from an aqueous precursor by flame-assisted spray pyrolysis. *J Eur Ceram Soc*. 2007;27:4489–4497.
24. Yen WM, Shionoya S, Yamamoto H. *Phosphor Handbook*, 2nd ed. Boca Raton: CRC Press Taylor & Francis Group, LLC, 2007.
25. FLUENT 6.3 User's Guide. Lebanon: FLUENT Inc., 1996.
26. Xiong Y, Lyons SW, Kodas TT, Pratsinis SE. Volatile metal oxide evaporation during aerosol decomposition. *J Am Ceram Soc*. 1995;78:2490–2496.
27. Lenggoro IW, Hata T, Iskandar F, Lunden MM, Okuyama K. An experimental and modeling investigation of particle production by spray pyrolysis using a laminar flow aerosol reactor. *J Mater Res*. 2000;15:733–743.
28. Widiyastuti W, Wang WN, Lenggoro IW, Iskandar F, Okuyama K. Simulation and experimental study of spray pyrolysis of polydispersed droplets. *J Mater Res*. 2007;22:1888–1898.
29. Perry HP, Green DW, Green D. *Perry's Chemical Engineers' Handbook*. USA: McGraw-Hill Companies Inc., 1999.
30. Purwanto A, Lenggoro IW, Chang H, Okuyama K. Preparation of submicron- and nanometer-sized particles of Y_2O_3:Eu^{3+} by flame spray pyrolysis using ultrasonic and two-fluid atomizers. *J Chem Eng Jpn*. 2006;39:68–76.
31. Johannessen T, Pratsinis SE, Livbjerg H. Computational fluid-particle dynamics for the flame synthesis of alumina particles. *Chem Eng Sci*. 2000;55:177–191.
32. Seto T, Hirota A, Fujimoto T, Shimada M, Okuyama K. Sintering of polydisperse nanometer-sized agglomerates. *Aerosol Sci Technol*. 1997;27:422–438.

Manuscript received Dec. 10, 2007, and revision received Sept. 8, 2008.